Influence of the applied stress rate on the stress corrosion cracking of 4340 and 3.5NiCrMoV steels under conditions of cathodic hydrogen charging

S. Ramamurthy [a,b,*], W.M.L. Lau [b], A. Atrens [a]

[a] Division of Materials, School of Engineering, University of Queensland, St. Lucia, QLD 4072, Australia
[b] Surface Science Western, The University of Western Ontario, London, Ontario, Canada N6G 0J3

ARTICLE INFO

ABSTRACT

Stress corrosion cracking (SCC) of as-quenched 4340 and 3.5NiCrMoV steels was studied under hydrogen charging conditions, with a cathodic current applied to the gauge length of specimens subjected to Linearly Increasing Stress Test (LIST) in 0.5 M H_2SO_4 solution containing 2 g/l arsenic trioxide (As_2O_3) at 30 °C. Applied stress rates were varied from 20.8 to 6×10^{-4} MPa s^{-1}. Both the fracture and threshold stress decreased with decreasing applied stress rate and were substantially lower than corresponding values measured in distilled water at 30 °C at the open circuit potential. The threshold stress values correspond to 0.03–0.08 σ_y for 4340 and 0.03–0.2 σ_y for the 3.5NiCrMoV steel. SCC velocities, at the same applied stress rate, were an order of magnitude greater than those in distilled water. However, the plots of the crack velocity versus applied stress rate had similar slopes, suggesting the same rate-limiting step. The fracture surface morphology was mostly intergranular, with quasi-cleavage features.

© 2011 Elsevier Ltd. All rights reserved.

1. Introduction

Stress Corrosion Cracking (SCC) [1–4] occurs for a susceptible material subjected to a tensile stress in an aggressive environment and can lead to catastrophic failures [5–8]. High strength steels are particularly susceptible; increasing yield strength significantly decreases the threshold stress intensity factor, K_{ISCC} [9–11]. As a consequence, SCC of high strength steels has been widely studied [12–17] and is an on-going effort [3,5,18–20]. This paper follows our previous studies of the SCC of two high-strength steels (4340 and 3.5NiCrMoV) in distilled water at 90 °C [21] and 30 °C [22], which studied the influence of the applied stress rate on SCC using the Linearly Increasing Stress Test (LIST) [23–31]. These studies indicated that the SCC velocity increased with increasing applied stress rate until it reached a maximum SCC velocity; for 4340, the maximum SCC velocity corresponded to the plateau SCC velocity measured in fracture mechanics tests [32,33]. The SCC velocity was the same for both steels, indicating a similar rate-limiting step. The experiments in distilled water at 30 and 90 °C indicated that the same rate-limiting step could be operating at both temperatures. Nevertheless, the mechanism of SCC could be different at the two temperatures. It was suggested [21,32,34] that the SCC mechanism involved anodic dissolution at 90 °C. Anodic dissolu-

tion, in its simplest form, involves the dissolution of metal at the crack tip, which is kept bare by the crack tip strain rate. In contrast, it was thought [32,33] that hydrogen was involved at temperatures less than 60 °C, in which case a role of crack tip strain rate is to maintain a bare crack tip for easy hydrogen entry into the steel. High strength steels exhibit intergranular fracture along prior austenite grain boundaries and hence it is difficult to identify the SCC mechanism from the fracture surface morphology alone [35].

The present research was carried out to explore the behaviour of these steels under cathodic hydrogen charging conditions using LIST. The LIST tests were the same as in our previous studies [21,22] so that the cracking behaviour with cathodic hydrogen charging could be directly compared with the experimental results in distilled water at 30 and 90 °C.

2. Experimental procedure

Cylindrical tensile specimens were machined from 4340 and 3.5NiCrMoV rotor steel from the same steel plates as used in our previous studies [21,22]. Their composition is shown in Table 1. All 4340 specimens were austenitized at 860 °C in high purity nitrogen for 1 h and quenched into oil. A similar procedure was followed for the 3.5NiCrMoV steel. Batch heat-treatment ensured that the microstructure was the same for each specimen for each steel. The heat treatment resulted in a fully martensitic microstructure in both steels, with a prior austenite grain size of 20 μm, as described by Gates et al. [36]. The yield strength (σ_y) of 4340 was 1700 MPa and that of the 3.5NiCrMoV steel was 1270 MPa.

* Corresponding author at: Surface Science Western, The University of Western Ontario, London, Ontario, Canada N6G 0J3. Tel.: +1 519 661 2173; fax: +1 519 661 3709.

E-mail address: sramamur@uwo.ca (S. Ramamurthy).

Table 1
Composition of the steels used in this study.

Steel	Composition (wt.%)								
	C	Ni	Cr	Mo	V	Mn	P	Si	S
4340	0.35	1.47	1.5	0.25	0.01	0.5	0.017	0.35	0.025
3.5NiCrMoV	0.23	3.05	1.9	0.65	0.07	0.45	0.011	–	0.009

After heat-treatment, each specimen was mounted in a lathe and the gauge section was ground through successive silicon carbide papers to 800 grit. Identical grinding conditions, including lathe speed, was employed for the preparation of each sample and, furthermore, the gauge section of each specimen was examined with optical microscopy after the grinding procedure to ensure that the gauge section surface was uniform and did not contain any coarse scratches or other surface defects that could act as crack initiation sites. The samples were then degreased in an ultrasonic cleaner with technical grade hexane solution, rinsed with distilled water and immediately loaded in the LIST apparatus.

The key to the LIST apparatus [23–31] is a lever beam. The specimen, and its loading train, is on one side of the lever beam and the other side contains a movable weight. Movement of the weight, driven by a synchronous motor, from its equilibrium position causes a proportional loading on the specimen, which is reported in terms of engineering stress. Synchronous motors of different speeds allowed nine applied stress rates, ranging from 0.0005 to 20 MPa s^{-1}.

For each LIST experiment, the steel was specimen immersed in 0.5 M H_2SO_4 solution containing 2 g/l arsenic trioxide (As_2O_3) at 30 °C as a hydrogen recombination poison. Each LIST specimen was subjected to a cathodic current of 0.5 A, resulting in a current density of 2600 A/m^2 on the gauge section. There was no surface damage or cracking on the tensile specimens in the as-charged condition without any applied stress. LISTs were conducted at 30 °C rather that at room temperature to ensure minimal variation in temperature. Once the desired temperature was reached, an hour was allowed for stabilisation and the cathodic current and stressing were applied. After fracture, the specimen was removed from the cell, washed with distilled water and dried. The fracture stress, σ_f, was calculated from the value of the load and the initial specimen cross-section area. The fracture surfaces were examined in a scanning electron microscope (SEM). Two identical samples were tested at each applied stress rate where there was SCC. Even at the low applied stress rates (0.0005 and 0.0006 MPa s^{-1}), where the duration of the tests could be a month or longer, repeat samples were used to determine the reproducibility of the measurements.

The SCC threshold stress, σ_{th}, was determined using a potential drop technique. During a LIST, a 5 A stabilised d.c. current (from a BWD model 245 A power supply) was applied to the specimen and the resulting potential drop across the specimen was plotted as a function of the applied stress. The threshold stress was identified as the stress at which there was a change in the slope in the potential drop versus applied stress plot, corresponding to a decrease in the cross-sectional area of the gauge section due to crack propagation. A CDP-10 linear displacement transducer (manufactured by Tokyo Sokki Kenkyujo Ltd.) was attached to the loading arms to measure the displacement of the specimen. This displacement was calibrated to give an output proportional to the specimen strain. The strain rate at the threshold stress was in each case determined from the slope of the strain versus time plot at the threshold stress; the threshold stress itself was evaluated from the potential drop measurements.

Assuming the SCC cracks grow at a constant rate between σ_{th} and σ_f, the average crack growth rate, v, was calculated from the following equation, where a is the maximum crack depth on the fracture surface after the test and $\dot{\sigma}$ is the applied stress rate [21,22]:

$$v = \frac{a\dot{\sigma}}{\sigma_f - \sigma_{th}} \tag{1}$$

The precision in the LIST tests were as follows. The total error in the specimen load was less than ±1% for loads of 1000 N and less than ±0.14% for higher loads [23]. The loading rate, determined by the speed of the synchronous motor, was accurate to ±1% [23]. The precision in the potential drop measurements was ±0.1 µV. Potential drop values were measured at every second for higher applied stress rates and at every few minutes for the low applied stress rates. The precision in the temperature control was better than ±1 °C. The error in the crack length measurements was ±0.1 mm [23].

3. Experimental results

3.1. Potential drop measurements

Figs. 1 and 2 present typical potential drop curves plotted against the applied stress for 4340 and 3.5NiCrMoV steel, respectively, subjected to LIST in 0.5 M H_2SO_4 + 2 g/l As_2O_3 solution under hydrogen charging conditions. The methodology employed during the potential drop measurements was the same as in previous studies [21,22]. Each number in Figs. 1 and 2 identifies the potential drop data for the LIST experiment with that same number in Figs. 3 and 4, respectively. Arrows in these figures marked the point at which there was a change in slope in the potential drop-applied stress plot. The stress at this point was identified as the threshold stress and plotted in Figs. 3 and 4.

3.2. Fracture stress and threshold stress

The threshold stress and the fracture stress for as-quenched 4340 under hydrogen charging conditions in 0.5 M H_2SO_4 + 2 g/l As_2O_3 solution at 30 °C are plotted in Fig. 3 as a function of applied stress rate. The symbols represent the experimental data and the black solid lines represent the polynomial regression fit for the data. SCC was observed at all applied stress rates shown in the figure. Moreover, both the fracture and threshold stresses decreased with decreasing applied stress rate. The fracture and threshold stress values were low. The fracture stress varied from ~200 to
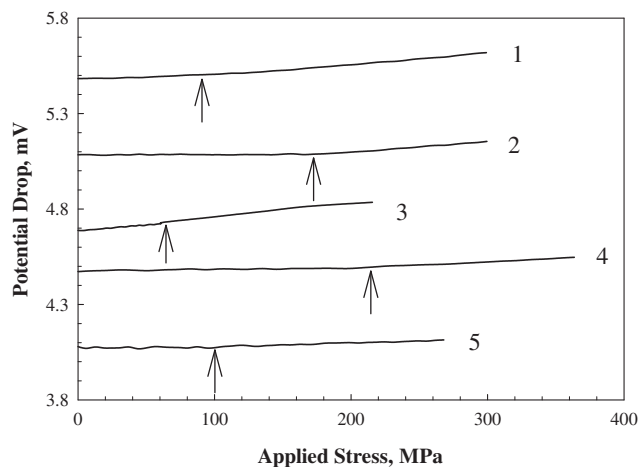

Fig. 1. A plot of the potential drop as a function of the applied stress for representative tests with as-quenched 4340. The arrows represent the change in the slope of potential drop plot and mark the threshold stress corresponding to crack initiation. Numbers 1–5 correspond to the data points shown in Fig. 3.
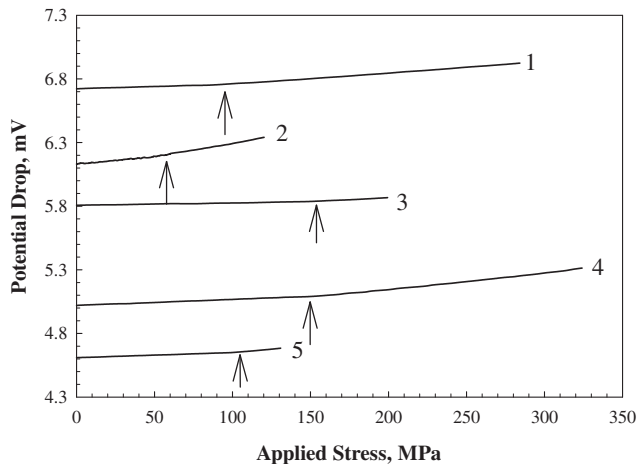
Fig. 2. A plot of the potential drop as a function of the applied stress for typical experiments with as-quenched 3.5NiCrMoV steel. Numbers 1–5 represent the corresponding data points in Fig. 4. The arrows mark the crack initiation point and correspond to the threshold stress.
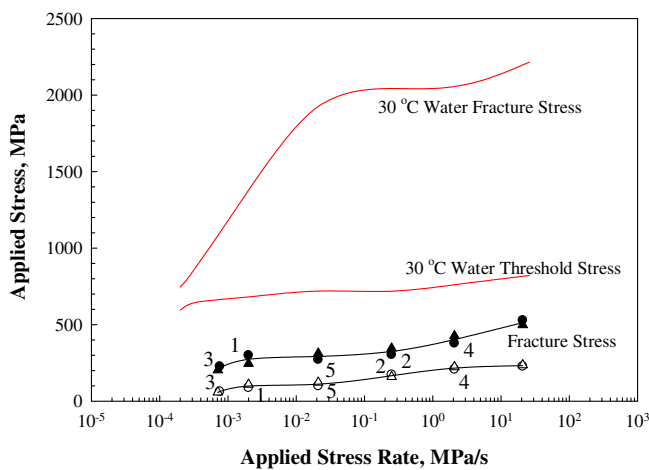

Fig. 3. A plot of fracture stress (closed symbols) and threshold stress (open symbols) plotted as a function of the applied stress rate for as-quenched 4340 under hydrogen charging condition at 30 °C. The numbers 1–5 correspond to the potential drop plots shown in Fig. 1. The red trend lines represent the polynomial regression data from the 30 °C water experiments [22]. (For interpretation of the references to colour in this figure legend, the reader is referred to the web version of this article.)

530 MPa and the threshold stress varied from ∼60 to 230 MPa. These values were much lower than the values measured in distilled water at 30 °C at the open circuit potential. The 30 °C water data has been plotted as red lines for comparison. This indicates that hydrogen charging has decreased the fracture and threshold stresses quite significantly, to less than one-third of the yield strength (1700 MPa) for the fracture stress and less than one-tenth of the yield strength for the threshold stress. Moreover, the results in 30 °C distilled water at the open circuit potential indicated that the fracture stress remained within a narrow band from 2 to 0.2 MPa s^{-1} and decreased significantly with further decrease in the applied stress rates. In contrast, the fracture stress decreased continuously with decreasing applied stress rate under hydrogen charging conditions.

Fig. 4 presents the results for as-quenched 3.5NiCrMoV steel. SCC had occurred at all applied stress rates shown in the figure. Also, both the fracture and threshold stresses decreased with decreasing applied stress rate, similar to the trends for 4340

(Fig. 3). For example, the fracture stress decreased from 418 MPa at higher applied stress rates to about 170 MPa at low applied stress rates. These values represent one-third to one seventh of the yield strength for this steel (1270 MPa). Similarly, the threshold stress decreased from 250 MPa at higher applied stress rates to ∼60 MPa at lower applied stress rates. Both 4340 and 3.5NiCrMoV steel exhibited similar threshold stresses at similar applied stress rates.

The trend lines for the 30 °C distilled water experiments at the open circuit corrosion potential were also plotted in this figure, presented by the red lines. Similar to the data for 4340, the distilled water experiments yielded higher fracture and threshold stress values than the hydrogen charging experiments. Moreover, SCC was not observed in 30 °C distilled water experiments at applied stress rates greater than 0.002 MPa s^{-1}. This is in contrast to the hydrogen charging experiments where there was SCC at all applied stress rates. These results again indicate that hydrogen charging was much more aggressive than measurements at open circuit corrosion potential. As discussed previously, in the water experiments, the mechanism of cracking could be anodic dissolution or hydrogen embrittlement. In this case, the availability of hydrogen is as a result of the cathodic reactions occurring near the vicinity of the crack tip. This reaction and the anodic dissolution (in anodic dissolution mechanism) are controlled by the crack tip strain rate (through the applied stress rate) which defines the frequency of the film rupture process. Hence, at higher applied stress rates, there is not sufficient time for the passive film formation and its rupture and this could result in the ductile fracture at higher applied stress rates. In contrast, under hydrogen charging conditions, there is a steady supply of hydrogen from cathodic charging which can diffuse ahead of the crack tip and can participate in the cracking process. This could explain why intergranular cracking was observed at all applied stress rates in this study.

For the 30 °C water experiments, the 4340 and 3.5NiCrMoV steel exhibited similar threshold stresses at lower applied stress rates. A similar trend was also observed for the hydrogen charging experiments, but the threshold stresses were much lower for the hydrogen charging experiments compared to the 30 °C water experiments.
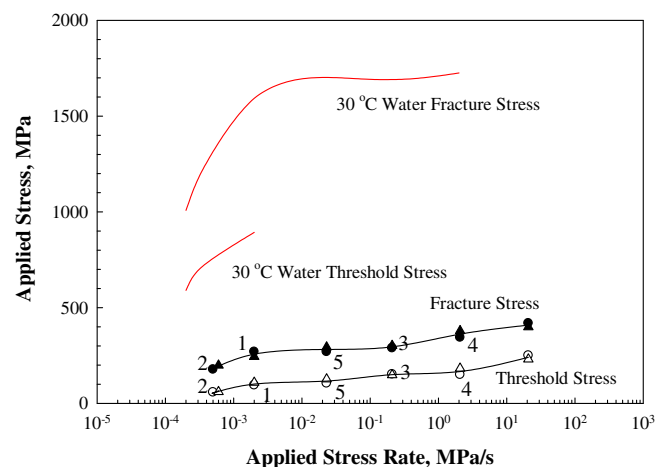

Fig. 4. A plot of fracture stress (closed symbols) and threshold stress (open symbols) plotted as a function of the applied stress rate for as-quenched 3.5NiCrMoV steel under hydrogen charging condition at 30 °C. The numbers 1–5 correspond to the potential drop plots shown in Fig. 2. The red trend lines represent the polynomial regression data from the 30 °C water experiments [22]. (For interpretation of the references to colour in this figure legend, the reader is referred to the web version of this article.)

3.3. Crack tip strain rate versus applied stress rate

The crack tip strain rates were calculated using two approaches as described in the prior papers [21,22]. The first approach was based on the assumption of a plane strain state at the crack tip [37]. Congleton et al. [37] showed that the crack tip strain rate $\dot{\varepsilon}_c$ at a distance x (in metres) from the tip of a growing crack in an ideally plastic solid under plane strain, small scale yielding conditions, large scale yielding and fully plastic conditions, is given by [37]:

$$\dot{\varepsilon}_c = \frac{\alpha L}{nx}(\dot{\varepsilon}_m - \dot{\varepsilon}_{NC}) + \frac{\beta \sigma_y v}{Ex}\left[\ln \frac{0.2E(\delta - \delta_{NC})}{n\sigma_y x}\right] \quad (2)$$

where α (= 0.5) is a constant, which was determined from the finite element analysis to be the same for stationary and growing cracks, L is the gauge length in metres, n is the number of circumferential cracks on the gauge section, $\dot{\varepsilon}_m$ and $\dot{\varepsilon}_{NC}$ are the strain rates acting on the specimen and on an uncracked gauge length, respectively, β is a constant with a value equal to 5.083 for a Poisson's ratio equal to 0.3, σ_y is the yield strength of the steel in MPa, v is the crack velocity in m s^{-1}, E is the Young's modulus in MPa, δ and δ_{NC} are the total displacement in metres for the cracked and the uncracked gauge length, respectively. The total elongation δ and the total crack mouth opening displacement δ_c, which may correspond to the crack opening displacement (after Congleton et al. [37]) were measured on several LIST specimens tested at various applied stress rates and the average values at each stress rate are shown in Table 2. Table 2 shows that the average δ_c values were 1.03×10^{-4} and 1.18×10^{-4} m for 4340 and the 3.5NiCrMoV steel, respectively. Similar to the 90 °C [21] and 30 °C [22] water results, the δ_c/δ ratio increased with decreasing applied stress rate. Table 2 implies that the mean values of $\dot{\varepsilon}_{NC}$ are 0.66 $\dot{\varepsilon}_{ext}$ and 0.66 $\dot{\varepsilon}_{ext}$ for 4340 and the 3.5NiCrMoV steels, respectively. Substituting these values, together with the values of α, β, the yield strength of the steels, the Young's modulus E = 210,000 MPa and choosing x = 5 × 10^{-5} m as an arbitrary choice (the value of x varies between 1×10^{-5} and 1×10^{-4} m {Congleton, Shoji and Parkins [37]}), Eq. (2) becomes:

$$\dot{\varepsilon}_c = \left[\frac{51}{n}\right]\dot{\varepsilon}_{ext} + 823 v \ln\left[\frac{51.5}{n}\right] \quad (3)$$

$$\dot{\varepsilon}_c = \left[\frac{52}{n}\right]\dot{\varepsilon}_{ext} + 615 v \ln\left[\frac{77.7}{n}\right] \quad (4)$$

for 4340 and the turbine rotor steel, respectively. In these equations, $\dot{\varepsilon}_{ext}$ is the strain rate resulting from the applied stress rate ($\dot{\varepsilon}_{ext} = \dot{\sigma}/E$).

The second approach for calculating the crack tip strain rate was based on the assumption of plane stress at the crack tip. Development of the model and the equations employed for the calculation of the crack tip strain rate were presented previously [21,22]. This model assumes plasticity at the crack tip and a crack tip stress equal to the yield strength. Moreover, as discussed [21,22], this model is partially based on the analysis of slow strain rate SCC data by Silcock [38]. As described in the model [21], the total measured strain (ε_m) is equal to the sum of the strain on the uncracked gauge length (ε_u) and the strain associated with stress corrosion cracks (ε_c). Assuming plasticity at the crack tip [$\sigma = K\varepsilon_c^{n_1}$], where K is a constant and n_1 is the strain hardening coefficient and determining the strain due to stress corrosion cracks and that from the uncracked gauge length [21], the equation for crack tip strain rate becomes:

$$\dot{\varepsilon}_c = \left[\frac{L\left[\varepsilon_m - \varepsilon_u + \frac{n\delta_c \varepsilon_u}{L}\right]}{n_1 n \delta_c \sigma_y}\right]\dot{\sigma} \quad (5)$$

where L corresponds to the length of the gauge section in metres, n is the number of cracks along the circumference of the gauge section, n_1 is the strain hardening coefficient, δ_c is the total crack

mouth opening displacement, σ_y is the yield strength and the parameters ε_m and ε_u have been described previously.

Unlike Eqs. (3) and (4), Eq. (5) does not contain either the SCC velocity or the macroscopic strain rate for the calculation of the crack tip strain rate. However, both ε_m and δ_c are affected by the SCC velocity and the SCC depth terms, and generally increase with an increase in either term. The macroscopic strain rate term is accounted for by the applied stress rate, which controls the macroscopic strain rate in the present study.

The crack tip strain rate values, calculated from both approaches (Eqs. (3) and (4) and Eq. (5)), are plotted in Fig. 5. Two more strain rates have also been plotted in this figure. The lowest line corresponds to the strain rate expected from $\dot{\varepsilon} = \dot{\sigma}/E$, where the strain rate has been calculated from the applied stress rate on the assumption of elastic deformation. The second line is the measured macroscopic strain rate, measured at the threshold stress as a function of applied stress rate. This strain rate was determined as the slope of the macroscopic strain versus time data. The solid lines in this figure represent the least square fit of the strain rate data to a relationship of the form $\dot{\varepsilon} = A_1 \dot{\sigma}^{m_1}$, where $\dot{\varepsilon}$ is the relevant strain rate, A_1 is a constant, m_1 is the slope of the corresponding straight line and $\dot{\sigma}$ is the applied stress rate. For the measured macroscopic strain rate data ($\dot{\varepsilon}_m$, measured at the threshold stress), the least square fit yields the following relationship. The fit parameters are shown in Table 3.

$$\dot{\varepsilon}_m = 1.0 \times 10^{-5}\dot{\sigma}^{1.01} \quad (6)$$

The open triangles and the crosses represent the crack tip strain rate $\dot{\varepsilon}_c$ calculated using Eqs. (3) and (4) based on the methodology described by Congleton et al. [37]. Least square fit of this data (solid lines through the symbols) yields the following relationship (Table 3):

$$\dot{\varepsilon}_c = 9.2 \times 10^{-3}\dot{\sigma}^{1.02} \quad (7)$$

The open squares and the circles have been based on the approach from Silcock [38] as described above (Eq. (5)). Least square fit of this data (solid lines through the symbols) yields the following relationship (Table 3):

$$\dot{\varepsilon}_c = 1.7 \times 10^{-4}\dot{\sigma}^{1.1} \quad (8)$$

Fig. 5 shows that the measured strain rate $\dot{\varepsilon}_m$ at the threshold stress is about a factor of two greater than the expected strain rate. Moreover, Fig. 5 shows that the crack tip strain rate calculated from both approaches were much greater than the expected or the measured strain rates. The ratio $\dot{\varepsilon}_c/\dot{\varepsilon}_m$ has values between 200 and 300 for approach 1 (Eqs. (3) and (4)) and this ratio appeared to be independent of the applied stress rate. For the crack tip strain rate calculations from approach 2 (Eq. (5)), the $\dot{\varepsilon}_c/\dot{\varepsilon}_m$ ratios were approximately 2000–3000, i.e. an order of magnitude greater than that from approach 1, and this ratio also appeared to be independent of the applied stress rate, i.e. the ratio of $\dot{\varepsilon}_c/\dot{\varepsilon}_m$ did not significantly change with the applied stress rate, i.e. the slopes for the lines $\dot{\varepsilon}_c$ and $\dot{\varepsilon}_m$ remained nearly parallel with increasing applied stress rate.

The relationship between the crack tip strain rate and the applied stress rate (Fig. 5) suggests that the crack tip strain rate was controlled by the applied stress rate. Similar slopes for the external macroscopic strain rate and the crack tip strain rates calculated form both approaches suggest that all these strain rates could be controlled by the applied stress rate or that the crack tip strain rate could be controlled by the external strain rate produced by the applied stress rate.

Table 3 also presents the fit parameters for the 90 °C [21] water and 30 °C [22] water experiments. The slopes for the crack tip strain rates from approach 2 [38, Eq. 5] were similar for water

Table 2
Average values of the total elongation δ and the total crack mouth opening displacement δ_c measured at various applied stress rates for as quenched 4340 and the 3.5NiCrMoV steel tested under hydrogen charging conditions at 30 °C.

Steel	Applied stress rate (MPa s^{-1})	No. of cracks observed along the gauge length, n	Total elongation δ ($\times 10^{-3}$ m)	Total crack mouth displacement δ_c ($\times 10^{-3}$ m)	δ_c/δ
4340	20.8	6	0.42	0.1	0.238
	20.8	4	0.4	0.08	0.2
	2.08	12	0.34	0.09	0.265
	2.08	8	0.3	0.08	0.267
	0.25	15	0.26	0.07	0.269
	0.25	10	0.28	0.08	0.286
	0.021	12	0.26	0.11	0.423
	0.021	11	0.24	0.09	0.375
	0.00208	16	0.29	0.13	0.448
	0.00208	15	0.28	0.11	0.429
	0.00076	21	0.33	0.16	0.485
	0.00071	24	0.34	0.14	0.412
	Mean		0.312 ± 0.056	0.103 ± 0.028	0.341 ± 0.097
Rotor	20.8	5	0.36	0.12	0.333
	20.8	4	0.41	0.14	0.341
	2.08	9	0.35	0.11	0.314
	2.08	10	0.38	0.13	0.342
	0.21	10	0.3	0.08	0.267
	0.21	11	0.33	0.09	0.273
	0.023	15	0.31	0.1	0.323
	0.023	13	0.29	0.09	0.31
	0.00208	24	0.34	0.13	0.382
	0.00208	22	0.31	0.11	0.355
	0.0005	29	0.35	0.15	0.429
	0.0006	32	0.38	0.17	0.447
	Mean		0.343 ± 0.036	0.118 ± 0.027	0.343 ± 0.055

experiments at both temperatures and the hydrogen charging experiments at 30 °C. This suggests that the crack tip strain rate is controlled by the applied stress rate in a similar manner for the experiments in water and under hydrogen charging. However, the slope for approach 1 [37, Eqs. 3 and 4] is slightly greater for the hydrogen charging experiments compared to the water experiments. This calculation takes into account the crack tip displacement values and could indicate that the crack tip displacement is affected in a slightly different manner under hydrogen charging compared to water experiments.

3.4. Crack velocity versus applied stress rate

Fig. 6 presents the average SCC velocity for both steels as a function of the applied stress rate. The SCC velocity was evaluated using Eq. (1). Fig. 6 shows that the SCC velocity was dependent on the applied stress rate for both steels. With increasing applied stress rate, the SCC velocity increased and the maximum SCC velocity measured was of the order of 1×10^{-4} m s^{-1}. Both steels exhibited similar maximum SCC velocities. Moreover, both 4340 and 3.5NiCrMoV steel exhibited similar SCC velocities (within an order of magnitude) at corresponding applied stress rates, which indicates that the SCC velocity was independent of the steel (composition and strength) and dependent only on the applied stress rate. Fig. 6 also shows that, at any applied stress rate, there is a scatter in SCC velocity by about a factor of two. The straight line in Fig. 6 is the least square fit of the data to the relation $v = A_2 \dot{\sigma}^{m_2}$, with the slope m_2 equal to 0.92 and A_2 is equal to 6.6×10^{-6}, a constant independent of applied stress rate. The fit parameters are also shown in Table 3. A similar value of slope (0.90) was obtained when the average SCC velocity was plotted against the external strain rate measured at the threshold stress, $\dot{\varepsilon}_m$ and fitted to the relation $v = A_3 \dot{\varepsilon}_m^{m_3}$ (Table 3) which again suggests that the external strain rate was dependent on the applied stress rate.

Fig. 7 presents the least square fit of the SCC velocity versus the applied stress rate for hydrogen charging condition and for the experiments in 30 °C [22] and 90 °C [21] distilled water at the open circuit potential. This figure shows the crack velocities under hydrogen charging conditions were greater than those in the 30 and 90 °C water experiments. Moreover, this difference appears to be slightly more pronounced at higher applied stress rates (>2 MPa s^{-1}). It should also be recalled that the 3.5NiCrMoV steel did not exhibit SCC in distilled water experiments at higher applied stress rates while cracking was observed at all applied stress rates under hydrogen charging conditions. For example, for the experiments in 30 °C distilled water, SCC was not observed at applied stress rates equal to or greater than 0.002 MPa s^{-1}. This also confirms the previous observation that hydrogen charging has enhanced the kinetics of SCC significantly, especially in the 3.5NiCrMoV steel. Despite the increase in SCC kinetics, the SCC velocity is still controlled by the applied stress rate, an observation similar to the results from 30 to 90 °C water experiments.

The results shown in Figs. 6 and 7 also indicate that the maximum SCC velocities for the 30 °C hydrogen charging experiments were of the order of $\sim 1.0 \times 10^{-4}$ m s^{-1} for both 4304 and 3.5NiCrMoV steels at higher applied stress rates. These values are much greater than the maximum SCC velocities for 30 °C water experiments, which were 1.1×10^{-9} m s^{-1} for the 3.5NiCrMoV steel and 7.3×10^{-6} m s^{-1} for the 4340 steel. In 30 °C water, SCC was not observed at applied stress rates greater than 2×10^{-3} MPa s^{-1} for the 3.5NiCrMoV steel, whilst there was cracking at all applied stress rates under hydrogen charging conditions. This again indicates that the SCC kinetics under hydrogen charging conditions is different from that at open circuit potential in 30 °C distilled water.

3.5. Crack velocity versus crack tip strain rate

Fig. 8 presents the SCC velocity plotted against the crack tip strain rate, calculated using the two approaches as discussed above. The closed symbols represent the data from the first approach (Eqs. (3) and (4)); the open symbols represent the second approach (Eq. (5)). The solid lines represent the least square fit of the data to the equation $v = A_4 \dot{\varepsilon}_c^{m_4}$, where m_4 is the exponent
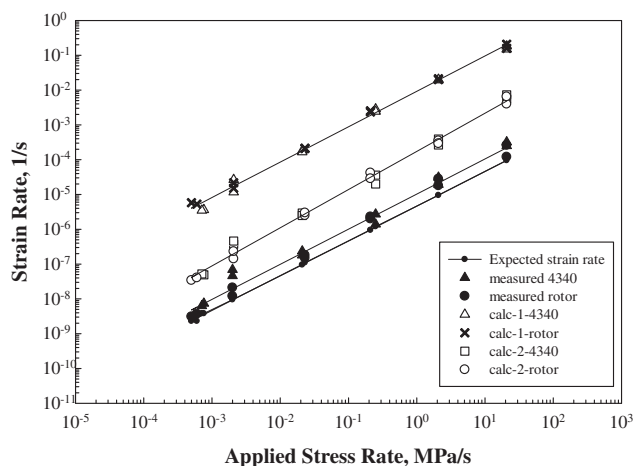
Fig. 5. Plots of strain rate as a function of the applied stress rate. The lowest line corresponds to the strain rate calculated from the applied stress rate on the assumption of elastic deformation. The full triangles and circles represent measurements of the macroscopic specimen strain rate, measured at the threshold stress as a function of the applied stress rate. The open symbols represent the crack tip strain rate evaluated based on the best existing literature approaches. The open triangles and crosses have been calculated using, respectively, Eqs. (3) and (4) using the method of Congleton et al. [37]. The open squares and circles have been calculated based on the approach of Silcock [38] using Eq. (6). The least square fit parameters are shown in Table 3.

and A_4 is the constant. The fit parameters are shown in Table 3. The exponent (m_4) values are 0.91 for approach 1 (Eqs. (3) and (4)) and 0.84 for approach 2 (Eq. (5)).

The data shown in Fig. 8 show that the SCC velocity was dependent on the crack tip strain rate and increased with increasing crack tip strain rate. Both the 4340 and the 3.5NiCrMoV steel had similar SCC velocities at corresponding crack tip strain rates. This observation is similar to the trends presented in the SCC velocity versus the applied stress rate plot shown in Fig. 7. In fact, the exponents in Fig. 7 and 8 (as shown in Table 3) are similar in value. Moreover, the value of the exponents suggests that the crack tip was under plane stress state for most of the test and was proportional to the applied stress rate.

Fig. 9 presents the least square fit for the hydrogen charging data (black lines) and the data from 30 °C (red lines) and 90 °C (blue lines) distilled water experiments under open circuit corrosion potential. The solid lines represent the plots from approach 1 (Eqs. (3) and (4)) and the dashed lines represent the plots from approach 2 (Eq. (5)). Comparison plots shown in this figure indicates that cracking is controlled by the strain rate, even under hydrogen charging conditions. However, the slope under hydrogen charging condition is slightly different from 30 to 90 °C distilled water, thus again confirming that cracking kinetics under hydrogen charging conditions are different from that in distilled water experiments.

3.6. Fractography

Figs. 10 and 11 present representative secondary scanning electron micrographs of fractures for 4340 and the 3.5NiCrMoV steel at various applied stress rates. Fig. 10 indicates that the fractography was similar for all applied stress rates, and that the applied stress rate did not influence the fracture morphology. The micrographs indicated that the fracture morphology was a mixed mode consisting of some intergranular fracture with a large amount of transgranular fracture, and with a significant amount of plasticity. Dimple rupture and slip steps could be clearly seen in these figures. The plasticity appeared to arise from the ductile overload region,

beyond the SCC region. Moreover, the grain facets appear to be relatively clean in the micrographs in Fig. 10. The corresponding micrographs for the 3.5NiCrMoV steel are shown in Fig. 11. These figures indicate that the fracture mode was mostly intergranular at low applied stress rates. However, the extent of transgranular features increased with increasing applied stress rate and at higher applied stress rates, it was mostly transgranular with a significant amount of plasticity; dimple rupture and slip steps could be clearly seen in these figures. Thus, it is possible that the failures at higher applied stress rates for the 3.5NiCrMoV steel could be due to a mixture of SCC and another mode of failure, while for 4340, it could be mainly due to SCC.

In the 30 °C water experiments at the open circuit potential, the fracture surface morphology was mixed mode containing intergranular fracture and transgranular features exhibiting significant amounts of plasticity. However, SCC was not observed at applied stress rates greater than 2×10^{-3} MPa s^{-1} for the 3.5NiCrMoV steel, while cracking was observed at all applied stress rates under hydrogen charging conditions. The difference in the fracture morphology at higher applied stress rates for this steel again suggests that the kinetics of cracking could be different under hydrogen charging conditions compared to the experiments in distilled water at open circuit potential.

4. Discussion

4.1. Fracture and threshold stress

The fracture stress measured in this study under hydrogen charging conditions varied between 200 and 528 MPa for 4340 and 198 to 419 MPa for the 3.5NiCrMoV steel. These fracture stress values correspond to 0.09–0.23 σ_{fo} for the 4340 steel and 0.11–0.25 σ_{fo} for the 3.5NiCrMoV steel where σ_{fo} is the fracture stress in air. These values are much lower than those for the experiments in 30 °C water [22], in which the fracture stress for the 4340 steel ranged from 0.3 to 0.95 σ_{fo} and 0.571 to 0.98 σ_{fo} for the 3.5NiCrMoV steel. Thus, these results indicate that the hydrogen charging has significantly decreased the fracture stress for both steels. Also, these values are lower than the extent of the decrease in fracture stress for the slow strain rate testing of hydrogen charged 4135 steel specimens (tensile strength 1450 MPa) [39]. In that study [39], the fracture stress decreased to ~0.3 σ_{fo} for the specimens containing 1.3 ppm diffused hydrogen. One difference between that study [39] and the current study is the dynamic charging employed in the current study, which means that the hydrogen fugacity would be much greater, consistent with the larger decrease in the fracture stress.

The threshold stress measured in this study varied between ~60 and 140 MPa for the 4340 steel and 50–250 MPa for the 3.5NiCrMoV rotor steel. These values correspond to 0.03–0.08 σ_y for 4340 and 0.03–0.2 σ_y for the 3.5NiCrMoV steel. These values are much lower than those in 30 °C water [22], namely 0.38–0.48 σ_y for 4340 and 0.43–0.73 σ_y for the 3.5NiCrMoV steel. This further confirms that the kinetics of cracking under hydrogen charging is different from that in 30 °C water.

Lijie et al. [40] have studied the hydrogen-facilitated SCC of 310 stainless steel and observed that hydrogen reduced the stability of the passive film and shortened the incubation of SCC. Moreover, this reduced initiation time and hydrogen-facilitated dissolution increased the crack growth rate and reduced the time to failure. As a result, a decrease in the threshold stress was observed in their study. A significant reduction in the threshold stress as a result of hydrogen charging was also observed in the present study; however the mechanism of cracking could be different in stainless steel compared to the high strength steels examined in this study.

Table 3
Parameters for the least square fit of the data reported in this study and the results from 30 to 90 °C water (at open circuit potential) experiments.

Data to be fitted	Relationship	Parameters under hydrogen charging condition at 30 °C		Parameters for 30 °C water [22]		Parameters for 90 °C water [21]	
		Constant A	Slope m	Constant A	Slope m	Constant A	Slope m
Measured strain rate versus applied stress rate	$\dot{\varepsilon}_m = A\dot{\sigma}^m$	1.0×10^{-5}	1.01	9.5×10^{-6}	1.01	1.9×10^{-5}	1.02
Calculated crack tip strain rate versus applied stress rate (calculation 1)	$\dot{\varepsilon}_c = A_1\dot{\sigma}^{m_1}$	9.2×10^{-3}	1.02	1.7×10^{-3}	0.85	3.4×10^{-3}	0.84
Calculated crack tip strain rate versus applied stress rate (calculation 2)	$\dot{\varepsilon}_c = A_1\dot{\sigma}^{m_1}$	1.7×10^{-4}	1.1	5.6×10^{-4}	1.06	5.9×10^{-4}	1.05
Stress corrosion crack velocity versus applied stress rate	$v = A_2\dot{\sigma}^{m_2}$	6.6×10^{-6}	0.92	3.4×10^{-4}	0.78	7.6×10^{-7}	0.78
Stress corrosion crack velocity versus measured strain rate	$v = A_3\dot{\varepsilon}_m^{m_3}$	2.1×10^{-1}	0.90	3.2×10^{-3}	0.73	1.4×10^{-2}	0.98
Stress corrosion crack velocity versus calculated crack tip strain rate (calculation 1)	$v = A_4\dot{\varepsilon}_c^{m_4}$	4.8×10^{-4}	0.91	1.4×10^{-4}	0.89	1.8×10^{-4}	0.74
Stress corrosion crack velocity versus calculated crack tip strain rate (calculation 2)	$v = A_4\dot{\varepsilon}_c^{m_4}$	9.3×10^{-3}	0.84	1.59×10^{-4}	0.73	1.6×10^{-4}	0.94

The results shown in Figs. 3 and 4 also indicate that the threshold stress decreased with decreasing applied stress rate. This is in contrast to the 30 °C water data [22], where for 4340 the threshold stress remained constant at higher applied stress rates and decreased with the applied stress rate at lower applied stress rates. The different behaviour under hydrogen charging could be attributed to the longer test duration at lower applied stress rates, which results in greater hydrogen concentrations within the steel due to the dynamic charging employed in this study. In fact, a plot of threshold stress versus logarithmic of the test duration or the total accumulated charge would yield a linear fit with the threshold stress decreasing proportionately with the accumulated hydrogen in the steel. Such behaviour has also been observed previously; Zhang et al. [41] observed such a linear relationship when hydrogen assisted cracking experiments were performed in high strength T-250 maraging steel.

4.2. Crack tip strain rate

The proposed role of crack tip strain rate varies depending on the mechanism of cracking. In the anodic dissolution mechanism, its function is to maintain the crack-tip bare so that metal dissolution can occur, which results in crack propagation. In the hydrogen embrittlement mechanism, the crack tip strain rate facilitates hydrogen production at the crack tip and also its transport to the region ahead of the crack tip for internal hydrogen. However, for the current set of experiments, hydrogen production is directly a result of cathodic charging and could be significant compared to the hydrogen production at the crack tip. Hence, the role of crack tip strain rate is to facilitate hydrogen transport to the regions ahead of the crack tip.

The data shown in Fig. 6 can be considered to represent the region I of a fracture mechanics tests, an observation similar to that for 90 °C water [21] and 30 °C water data [22]. This suggests that in region I of the SCC velocity–stress intensity factor plot, the SCC velocity is controlled by the crack tip deformation behaviour. Assuming that the SCC velocity in region I is indeed controlled by crack tip deformation, the minimum SCC velocity observed by Magdowski [32,33] for 4340 in room temperature water was 1×10^{-10} m s^{-1}. By extrapolating the least square fit line in Fig. 6 to this minimum SCC velocity, the critical applied stress rate below which cracking SCC would not occur in 4340 can be determined. This extrapolation indicates a value of approximately 1×10^{-5} MPa s^{-1} for the critical applied stress rate. This value is somewhat similar to the value of 2.6×10^{-5} MPa s^{-1} reported for the 30 °C water data [22]. It should also be mentioned that the extrapolation is applicable only to the experiments under hydrogen charging conditions. In addition, if experiments were to be performed at applied stress rates lower than those employed in this

study, it is possible that specimens would exhibit SCC at the very low applied stress rates resulting in the minimum crack velocity below which SCC could not occur much lower than that is shown in the present study.

Using the critical applied stress rate value, the critical applied strain rate, below which SCC would not occur, can be determined from Fig. 5. Extrapolating the least square fit line in Fig. 5 to this critical applied stress rate of 1×10^{-5} MPa s^{-1}, predicts a value of the critical crack tip strain rate of 9.0×10^{-8} s^{-1} from approach 1 (Eqs. (3) and (4)) and 8.0×10^{-10} s^{-1} from approach 2 (Eq. (5)). During LIST, the stress state acting at the crack tip varies from plane stress for most of the test to plane strain at final stages of fracture. Hence, the actual critical crack tip strain rate would lie in between these two values. The upper limits of the crack tip strain rates, above which SCC could not occur, were 0.2 and 8×10^{-3} s^{-1}, corresponding to the applied stress rates of 2.6×10^1 MPa s^{-1} for the 3.5NiCrMoV rotor steel and 3.0 and 5×10^{-2} s^{-1} corresponding to an applied stress rate of ~2.0×10^2 MPa s^{-1} for 4340.

4.3. Effect of hydrogen charging on kinetics of cracking

The results presented in this study, especially the correlation between the applied stress rate and the SCC velocity (Fig. 6), indicate that the SCC velocity increased with increasing applied stress rates for both steels. The maximum SCC velocity in the present study was 8.5×10^{-5} m s^{-1} for 4340 and 1.0×10^{-4} m s^{-1} for the 3.5NiCrMoV steel. These values show some interesting trends. Firstly, the maximum SCC velocity is independent of the yield strength of the steel under hydrogen charging conditions. This is in contrast to the 30 °C water experiments, in which the maximum SCC velocity was dependent on the yield strength of the steel [22]. Secondly, it is possible that we may not have reached the plateau crack velocity (v_{II}) in LIST tests, at least for 4340. The maximum SCC velocity in this study for the 3.5 NiCrMoV steel correlated with the v_{II} observed in gaseous hydrogen for steel with similar yield strength [42]. However, for a steel of ~1700 MPa yield strength, the plateau crack velocity, v_{II}, was in excess of 1×10^{-4} m s^{-1}, which was greater than the crack velocities observed in this study.

The results presented in the previous sections indicated that the relationship between the SCC velocity and the crack tip strain rate calculated from both approaches can be described by the equation: $v = A_4\dot{\varepsilon}_c^{m_4}$, where A_4 and m_4 are constants. As shown in Table 3, the value of the exponent was 0.91 and 0.84 for the hydrogen charging experiments and these values were similar to those for the 90 and 30 °C results (also shown in Table 3). As discussed, these values were greater than those reported for the SCC of stainless steels (0.3–0.5) in high temperature water [43–46], but are within the range 0.5–1 reported for sensitised stainless steels in high
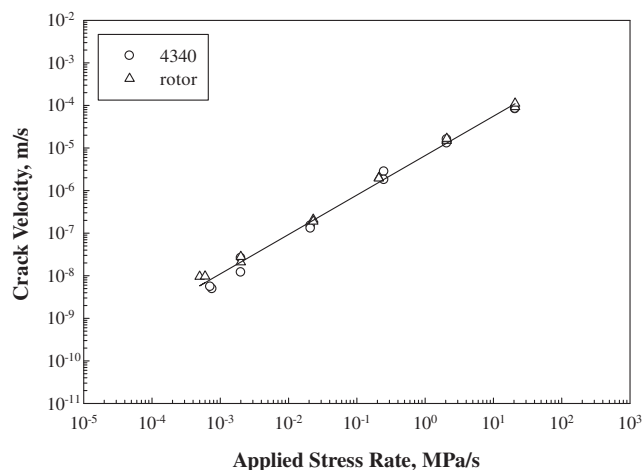
Fig. 6. Average crack velocity plotted as a function of applied stress rate for both steels under hydrogen charging condition at 30 °C. The least square fit parameters are shown in Table 3.
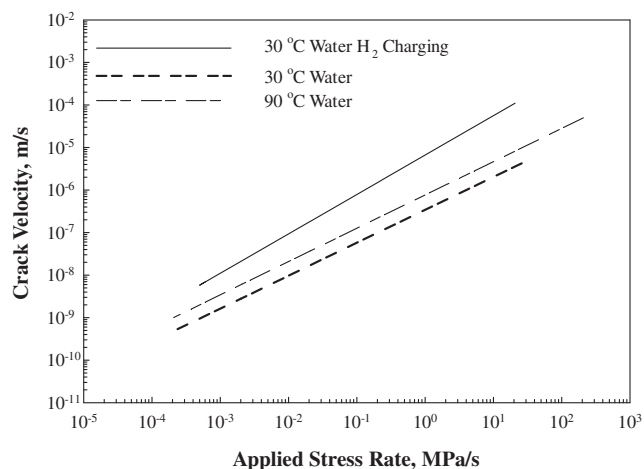

Fig. 8. Average crack velocity plotted as a function of crack tip strain rate (shown in Fig. 5) for both steels under hydrogen charging condition at 30 °C. Crack tip strain rate from approach 1 (Eqs. (3) and (4)) and approach 2 (Eq. (5)) have been plotted in this figure. The least square fit parameters are shown in Table 3.

Fig. 7. Linear square fit plots of average stress corrosion crack velocity as a function of applied stress rate under hydrogen charging condition at 30 °C (solid line), at open circuit potential in 30 °C water (medium dash line) [22] and at open circuit potential in 90 °C water (dark dash line) [21] for both steels. The least square fit parameters are shown in Table 3.

Fig. 9. Comparison of the least square fit data under hydrogen charging condition at 30 °C (black) and at open circuit potentials (OCP) in 30 °C (red) [22] and 90 °C (blue) [21] water based on approach 1 (Eqs. (3) and (4) – solid line) and approach 2 (Eqs. (5) – dash line). The least square fit parameters are shown in Table 3. (For interpretation of the references to colour in this figure legend, the reader is referred to the web version of this article.)

temperature water [47]. Moreover, typical slopes for log v versus log $\dot{\varepsilon}$ plots were of the order of 0.5–0.7 for intergranular SCC (IGSCC) and 0.2–0.3 for transgranular (TGSCC) [48]. Thus, the parameters from this study are similar to the range reported in previous studies. Moreover, the fact that the data from this study follow this relationship indicates that the crack tip plasticity controls the events at the crack tip. Crack tip plasticity could control the processes affecting the hydrogen transport to the crack tip, such as the dislocation motion and pile up at the crack tip. In addition, the crack tip plasticity could also control the film rupture events thus creating a bare metal region, which would also facilitate some corrosion at the crack tip and would facilitate hydrogen entry.

The data shown in Fig. 8 show that the SCC velocity was dependent on the crack tip strain rate and increased with increasing crack tip strain rate, except for the 3.5NiCrMoV steel at higher crack tip strain rates. Both the 4340 and the 3.5NiCrMoV steel specimens exhibited similar SCC velocities at corresponding crack tip strain rates. The exponents in Fig. 7 and 8 (as shown in Table 3) have similar values. These observations indicate that the crack velocity was dependent only on the applied stress/strain rate and was indepen-
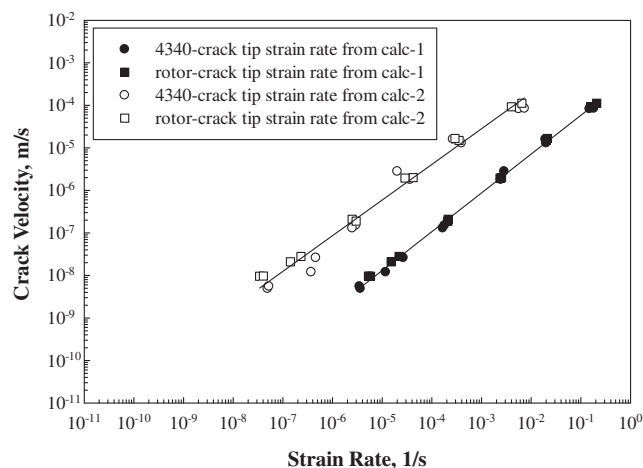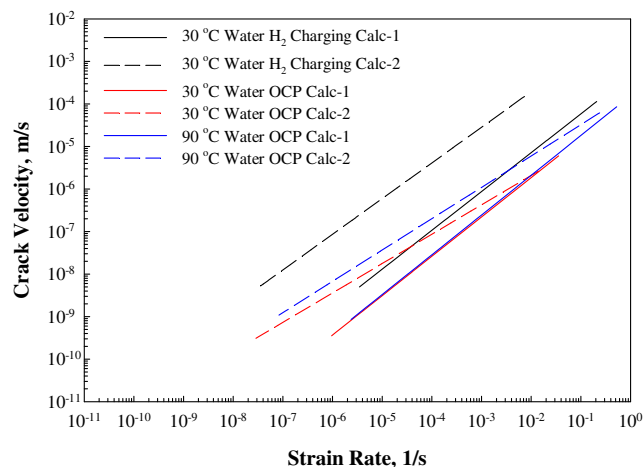
dent of the composition of the steels used in the present study. Because the microstructure is fully martensitic for both steels [36], the crack velocity also appeared to be independent of the microstructure. This trend is similar to the results from the previous data from the 90 °C [21] and 30 °C [22] water experiments and is also analogous to that observed in region I of the fracture mechanics tests for these steels in high temperature water [49] where the experimental data for these steels lie on the same vertical band. Such observation has also been substantiated by the extensive study conducted by the same group [50]. These observations imply a similar rate-limiting step, independent of steel composition for both steels, could be responsible for the crack growth.

The nature of the rate-limiting step is important. For the experiments in water and under anodic dissolution mechanism, Scully [51], Newman [52] and others [53–55] suggested that the role of the crack tip strain is to rupture the passive film at the crack tip to facilitate metal dissolution and crack propagation. For the current study, under hydrogen charging conditions, the rupture event at the crack tip may not be the rupture of a passive film, but merely
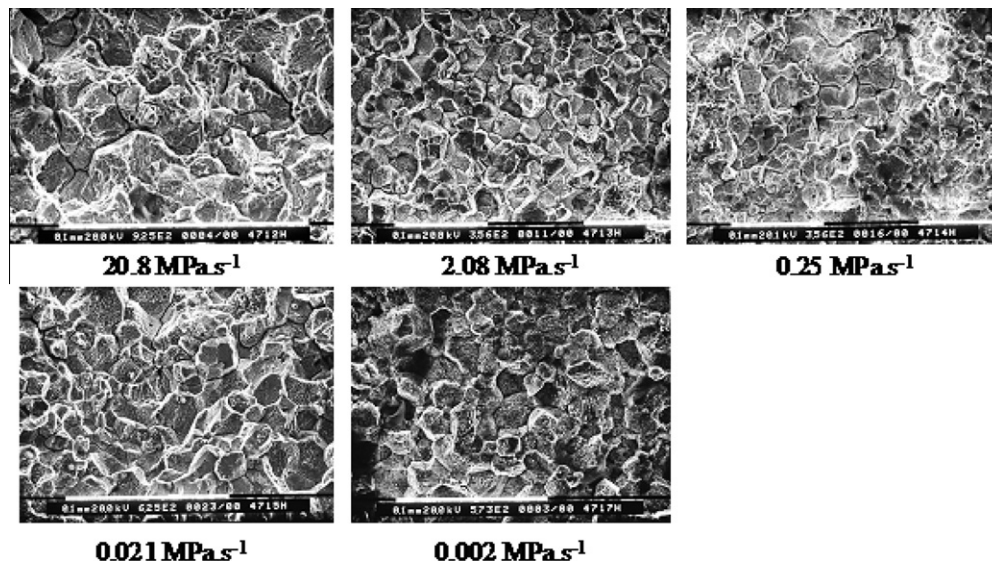
Fig. 10. Representative secondary electron micrographs showing the fracture surface morphology from the LIST experiments under hydrogen charging condition at 30 °C for 4340 at various applied stress rates.
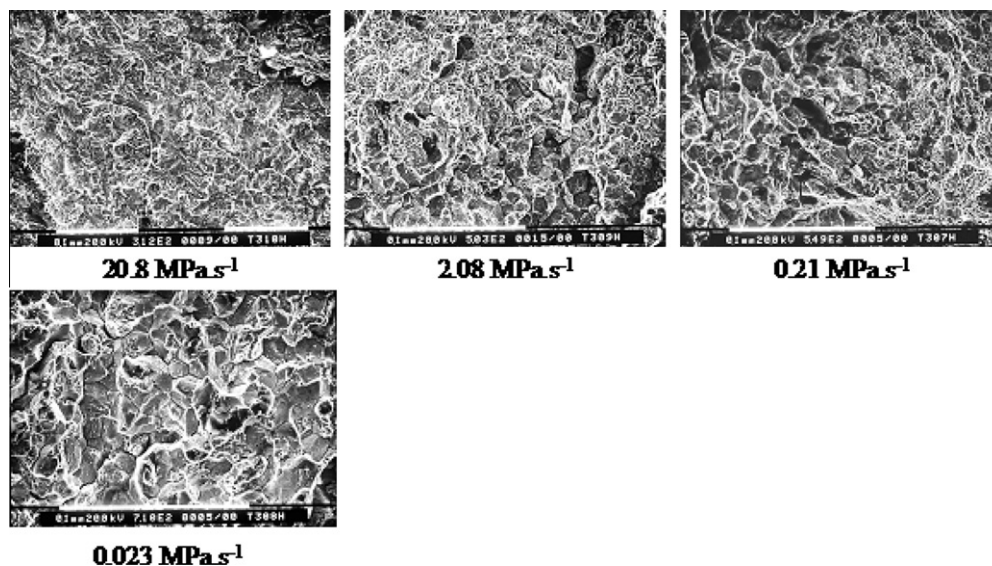

Fig. 11. Representative secondary electron micrographs showing the fracture surface morphology from the LIST experiments under hydrogen charging condition at 30 °C for the 3.5NiCrMoV steel at different applied stress rates where there was SCC.

the rupture of a surface film that hinders hydrogen ingress into the region ahead of the crack tip. Thus, the rate-limiting step would be expected to be the same for both steels in the current set of experiments. The role of the applied stress rate is to produce a crack tip strain rate above the critical crack tip strain rate required for film rupture. The increase in the crack tip strain rate through the increase in the applied stress rate could increase the film rupture rate and hence accelerate the hydrogen diffusion and transport processes occurring at regions ahead of the crack tip. Because the hydrogen is generated externally and not produced as a result of film rupture at the crack tip, the role of crack tip strain rate is to aid in the hydrogen transport and diffusion processes only. Thus, it is conceivable that the increase in the crack tip strain rate would increase the hydrogen diffusion/transport rate further, thus resulting in greater crack velocities. This possibility is also confirmed by the results shown in Figs. 6 and 8 in which the maximum crack velocities were much greater than those reported for 90 °C [21]

and 30 °C [22] water experiments and were similar for both steels independent of the steel composition. These observations can also explain why the plateau crack velocity (v_{ll}) may not have been reached in the current set of measurements.

The role of crack tip strain rate in facilitating hydrogen transport is also supported by the work of Scully and Moran [56]. Their study focused on the effect of mechanical strain on hydrogen entry and transport in 4340 under cathodic polarisation. Their data support the possibility of mechanical strain promoting enhanced hydrogen absorption as a result of film rupture. Rupture of the surface film enhanced the overall rate of hydrogen entry by increasing the hydrogen surface coverage and possibly the adsorption–absorption rate constant on the bare surfaces formed. They have also determined that the rate of hydrogen accumulation at a region ahead of the crack tip is controlled by the transport process. Their findings are also consistent with the results from this study in which the role of crack tip strain rate appeared to produce a bare

surface and enhance the transportation of hydrogen into the region ahead of the crack tip.

4.4. Fractography

Figs. 10 and 11 indicate that the fracture morphology was intergranular in both steels. There was some ductile fracture and plasticity in the 3.5NiCrMoV steel at the higher applied stress rates. Mostly intergranular fracture suggests that the preferential crack path could be along the prior austenite grain boundaries. This observation is consistent with the intergranular cracking model presented by Rieck [34,57], which proposes that the crack path is defined by the surface where most dislocations meet. Other than the slip steps (as shown in some of the micrographs in Figs. 10 and 11), the next obstacle the dislocations meet is the grain boundary. In low alloy steels, the prior austenite grain boundaries are high angle grain boundaries and present a more significant obstacle to dislocation motion than the low angle twin boundaries in martensite. This pile up of dislocations at the prior austenite grain boundaries produces a concentration of ledges and leads to dissolution of these ledges, causing cracking to be intergranular.

Another possible mechanism of intergranular cracking is the growth and the rupture of oxide films, as proposed by Atrens and Wang [58]. Using environmental SEM (ESEM), they observed that, for 4340 in distilled water, an oxide film was found to form on the surface of 4340 specimens after immersion in water. Applied stress was found to accelerate the oxide growth and the presence of small cracks within the oxide layer provided the pathway for the water to reach the bare metal. If the cracks were along the grain boundaries, then there was crack initiation along the grain boundaries. In their study, they observed that the extent of corrosion was determined by the competing processes of film cracking and repassivation. In the current study, any cracks in the oxide film are expected to facilitate hydrogen absorption and transport into the regions ahead of the crack tip. Thus, the role of the applied stress rate would be to increase the frequency and the extent of cracking in the oxide film at the crack-tip, thus increasing the rate of hydrogen availability at the regions ahead of the crack-tip. Such a possibility is also consistent with the observations by Scully and Moran [56].

The presence of intergranular cracking under hydrogen charging was also observed by Wang et al. [39]. In their study, crack initiation occurred at the centre of the specimen and propagated towards the outside surface. The very outer surface layers exhibited shear lips, the width of which decreased with increased hydrogen diffusion rate. Such observations were also found in the present study, where the fracture was mostly intergranular at most of the fracture surface and the extent of intergranular cracking, especially for the 3.5NiCrMoV steel, increased with decreasing applied stress rate (which provided longer times for hydrogen diffusion and resulting in increased hydrogen concentrations within the material).

5. Conclusions

LISTs were performed on as-quenched 4340 and 3.5NiCrMoV steels under hydrogen charging conditions in 0.5 M H_2SO_4 solution with 2 g/l arsenic trioxide (As_2O_3) at 30 °C. The experimental results indicate that:

(1) Cracking was observed at all applied stress rates under hydrogen charging conditions for both steels. This is in contrast to the experiments in 90 and 30 °C distilled water at open circuit potential where cracking was not observed at higher applied stress rates.

(2) The fracture stress values in the current study correspond to 0.09–0.23 σ_{fo} for 4340 steel and 0.11–0.25 σ_{fo} for the 3.5NiCrMoV steel (σ_{fo} is the fracture stress in air). These values are much lower than those for the experiments in 30 °C water [22], in which the fracture stress for 4340 ranged from 0.3 to 0.95 σ_{fo} and 0.571 to 0.98 σ_{fo} for the 3.5NiCrMoV steel.

(3) The dynamic charging decreased the fracture stress much more dramatically than that observed previously.

(4) The threshold stress values decreased significantly compared to the experiments in distilled water.

(5) Both the fracture stress and the threshold stress were dependent on the applied stress rate for both steels

(6) The measured SCC velocity increased with increasing applied stress rate. Both steels exhibited a similar SCC velocity at the same applied stress rate. Cracking was observed at higher applied stress rates in the 3.5NiCrMoV steel in contrast to the results from distilled water experiments.

(7) The measured SCC velocity was independent of the steel composition, indicating a similar rate-limiting step, independent of steel composition for both steels.

(8) Exponents of the least square fit data from this study were similar to those from 30 °C [22] and 90 °C [21] water experiments, indicating that the same rate limiting step could be operating in all three sets of experiments.

(9) Fracture surface morphology was mostly intergranular fracture, with significant amount of plasticity observed at higher applied stress rates.

6. List of symbols and abbreviations

SCC	stress corrosion cracking
IGSCC	intergranular stress corrosion cracking
TGSCC	transgranular stress corrosion cracking
LIST	linearly Increasing Stress Test
K_{ISCC}	threshold stress intensity
$\dot{\sigma}$	applied stress rate
σ_f	fracture stress
σ_{thi}	threshold stress
σ_{fo}	fracture stress in air
σ_y	yield strength, in MPa
v	crack velocity
ε_m	total measured strain, sum of the strain associated with cracks (ε_c) and the strain on the uncracked gauge length (ε_u)
$\dot{\varepsilon}_{ext}$	external strain rate resulting from the applied stress rate
$\dot{\varepsilon}_m$	strain rate acting on the specimen
$\dot{\varepsilon}_{NC}$	strain rate acting on the uncracked gauge length
$\dot{\varepsilon}_c$	crack tip strain rate at a distance x from the crack tip
δ	total elongation
δ_c	total crack mouth displacement
δ_{NC}	total displacement for the uncracked gauge length
α	constant
L	gauge length in m
n	number of circumferential cracks in the gauge section
β	constant (5.083) for Poisson ratio = 0.3
K	constant
n_1	strain hardening coefficient
E	Young's modulus

References

[1] W.R. Warke, Stress-corrosion cracking, in: W.T. Becker, R.J. Shipley (Eds.), ASM Handbook, Failure Analysis and Prevention, vol. 11, ASM, Metals Park, Ohio, 2002, pp. 823–860.

[2] W. Dietzel, Stress corrosion cracking in metals, in: K.H.J. Buschow, R.W. Cahn, M.C. Flemings, B. Ilschner, E.J. Kramer, S. Mahajan (Eds.), Encyclopedia of Materials: Science and Technology, Elsevier Science Ltd., Amsterdam, 2001, p. 8883.

[3] B.Y. Fang, A. Atrens, J.Q. Wang, E.H. Han, Z.Y. Zhu, W. Ke, Review of stress corrosion cracking of pipeline steels in "Low" and "High" pH solutions, J. Mater. Sci. 38 (2003) 127–132.

[4] N. Winzer, A. Atrens, G. Song, E. Ghali, W. Dietzel, K.U. Kainer, N. Hort, C. Blawert, A critical review of the stress corrosion cracking (SCC) of magnesium alloys, Adv. Eng. Mater. 7 (2005) 659–693.

[5] R.P. Gangloff, Hydrogen assisted cracking of high strength alloys, in: I. Milne, R.O. Ritchie, B. Karihaloo (Eds.), Comprehensive Structural Integrity, J. Petit, P. Scott (vol. Eds.), vol. 6, Elsevier Science, New York, NY, 2003, pp. 31–101.

[6] J.M. Hodge, I.L. Mogford, UK experience of stress corrosion cracking in steam turbine discs, Proc. Inst. Mech. Eng. 96 (1979) 193.

[7] D. Kalderon, Design of large steam turbines for fossil and nuclear power stations, Proc. Inst. Mech. Eng. 186 (1972) 341.

[8] C. Liu, D.D. Macdonald, Prediction of failures of low-pressure steam turbine disks, J. Pressure Vessel Technol. 119 (1997) 393.

[9] W.W. Gerberich, N.I. Tymiak, J. Jungk, T. Wyrobek, Hydrogen effects on material behaviour and corrosion deformation interactions, in: N.R. Moody, A.W. Thompson, R. Ricker, G. Was, R. Jones (Eds.), Proceedings of the International Conference on Hydrogen Effects on Material Behaviour and Corrosion Deformation Interactions, Minerals, Metals and Materials Society, Warrendale, PA, 2003, pp. 153–164.

[10] P.G. Marsh, W.W. Gerberich, Stress corrosion cracking of high strength steels, in: R.H. Jones (Ed.), Yield Strengths Greater Than 1240 MPa, ASM International, Metals Park, Ohio, 1992, pp. 63–90.

[11] S. Pyun, H.-K. Lee, Effect of threshold stress intensity on fracture mode transitions for hydrogen-assisted cracking in AISI 4340 steel, Metall. Trans. A 21A (1990) 2577–2583.

[12] H.L. Li, K.W. Gao, L.J. Qiao, Y.B. Wang, W.Y. Chu, Strength effect in stress corrosion cracking of high-strength steel in aqueous solution, Corrosion 57 (2001) 295–299.

[13] N. Eliaz, A. Shachar, B. Tal, D. Eliezer, Characteristics of hydrogen embrittlement, stress corrosion cracking and tempered martensite embrittlement in high-strength steels, Eng. Fail. Anal. 9 (2002) 167–183.

[14] W.Y. Maeng, J.H. Lee, U.C. Kim, Environmental effects on the stress corrosion cracking susceptibility of 3.5NiCrMoV steels in high temperature water, Corros. Sci. 47 (2005) 1876–1895.

[15] W.Y. Maeng, D.D. Macdonald, The effect of acetic acid on the stress corrosion cracking of 3.5NiCrMoV turbine steels in high temperature water, Corros. Sci. 50 (2008) 2239–2250.

[16] S.P. Lynch, Progress towards Understanding Mechanisms of Hydrogen Embrittlement and Stress Corrosion Cracking, Paper 07493, Corrosion 2007, NACE Press, Houston, 2007, pp. 074931–0749355.

[17] T. Nakayama, Stress corrosion cracking of carbon steels and low alloy steels, Weld. Int. 21 (2007) 89–94.

[18] E. Villalba, A. Atrens, SCC of commercial steels exposed to high hydrogen fugacity, Eng. Fail. Anal. 15 (2008) 617–641.

[19] A. Turnbull, S. Zhou, Steam turbines part 2-stress corrosion cracking of turbine disc steels, Corros. Eng. Sci. Technol. 38 (2003) 177–191.

[20] S. Zhou, Environment Assisted Cracking of Turbine Blade Steels – A Review, NPL Report, DEPC-MPE 033, March 2007.

[21] S. Ramamurthy, A. Atrens, The stress corrosion cracking of as-quenched 4340 and 3.5NiCrMoV steels under stress rate control in distilled water at 90 °C, Corros. Sci. 34 (1993) 1385–1402.

[22] S. Ramamurthy, A. Atrens, The influence of applied stress rate on the SCC of 4340 and 3.5 NiCrMoV steels in distilled water 30 °C, Corros. Sci. 52 (2010) 1042–1051.

[23] A. Atrens, C.C. Brosnan, S. Ramamurthy, A. Oehlert, I.O. Smith, Linearly increasing stress test (LIST) for SCC research, Meas. Sci. Technol. 4 (1993) 1281–1292.

[24] N. Winzer, A. Atrens, W. Dietzel, V.S. Raja, G. Song, K.U. Kainer, Characterisation of stress corrosion cracking (SCC) of Mg–Al alloys, Mater. Sci. Eng. A 488 (2008) 339–351.

[25] N. Winzer, A. Atrens, W. Dietzel, G. Song, K.U. Kainer, Comparison of the linearly increasing stress test and the constant extension rate test in the evaluation of transgranular stress corrosion cracking of magnesium, Mater. Sci. Eng. A 472 (2008) 97–106.

[26] J.Q. Wang, A. Atrens, Analysis of service stress corrosion cracking in a natural gas transmission pipeline, active or dormant?, Eng Fail. Anal. 11 (2004) 3–18.

[27] J.Q. Wang, A. Atrens, SCC initiation for X65 pipeline steel in the "High" pH carbonate/bicarbonate solution, Corros. Sci. 45 (2003) 2199–2217.

[28] A. Atrens, A. Oehlert, Linearly increasing stress testing of carbon steel in 4 N NaNO$_3$ and in Bayer liquor, J. Mater. Sci. 33 (1998) 783–788.

[29] Z.F. Wang, A. Atrens, Initiation of stress corrosion cracking for pipeline steels in a carbonate–bicarbonate solution, Metall. Mater. Trans. A 27A (1996) 2686–2691.

[30] A. Oehlert, A. Atrens, Stress corrosion crack propagation in AerMet 100, J. Mater. Sci. 33 (1998) 775–781.

[31] J. Salmond, A. Atrens, SCC of copper using the linearly increasing stress test, Scripta Metall. Mater. 26 (1992) 1447–1450.

[32] R.M. Magdowski, SCC of Low Alloy Steel in Water, D. Tech. Sc. Thesis, Swiss Federal Institute of Technology, Zurich, 1987.

[33] M.O. Speidel, R.M. Magdowski, Stress corrosion cracking of steam turbine steels – an overview, in: J.T.A. Robert, J.R. Weeks, G. Theus (Eds.), Proceedings of the Second International Symposium on Environmental Degradation of Materials in Nuclear Power Systems – Water Reactors, American Nuclear Society, La Grange Park, 1986, pp. 267–275.

[34] R.M. Rieck, A. Atrens, I.O. Smith, The role of crack tip strain rate in the stress corrosion cracking of high strength steels in water, Metall. Trans. A 20A (1989) 889–895.

[35] S.P. Lynch, Failures of structures and components by environmentally assisted cracking, Eng. Fail. Anal. 1 (1994) 77–90.

[36] J.D. Gates, A. Atrens, I.O. Smith, Microstructure of as-quenched 3.5NiCrMoV Rotor steel: I. General structure and retained austenite, Z. Werkst. 18 (1987) 165–170.

[37] J. Congleton, T. Shoji, R.N. Parkins, The stress corrosion cracking of reactor pressure vessel steel in high temperature water, Corros. Sci. 25 (1985) 633–650.

[38] J.M. Silcock, Analysis of slow strain rate stress-corrosion data, Corros. Sci. 21 (1981) 723–730.

[39] M. Wang, E. Akiyama, K. Tsuzaki, Effect of hydrogen on the fracture behavior of high strength steel during slow strain rate test, Corros. Sci. 49 (2007) 4081–4097.

[40] Q. Lijie, C. Wuyang, M. Huijun, X. Jimei, G. Peixin, Hydrogen-facilitated corrosion and stress corrosion cracking of austenitic stainless steel of type 310, Metall. Trans. A 24A (1993) 959–962.

[41] Y.P. Zhang, D.M. Shi, W.Y. Chu, L.J. Qiao, Y.L. Shi, S.L. Zheng, S.B. Wang, Hydrogen-assisted cracking of T-250 maraging steel, Mater. Sci. Eng. A 417 (2007) 34–37.

[42] H.G. Nelson, D.P. Williams, Quantitative observations of hydrogen induced slow crack growth in a low alloy steel, in: J.E. Slater (Ed.), NACE-5 SCC and Hydrogen Embrittlement of Iron based Alloys, NACE, Houston, 1977, pp. 390–404.

[43] F.P. Ford, P.W. Emigh, Prediction of the maximum corrosion fatigue crack propagation rate in the low alloy steel-de-oxygenated water system at 288 degree C, Corros. Sci. 25 (1985) 673–692.

[44] P.S. Maiya, W.J. Shack, Effects of nominal, crack-tip strain rate on IGSCC susceptibility in cert tests, in: R.P. Gangloff (Ed.), Embrittlement by the Localized Crack Environment, The Metallurgical Society – AIME, Warrendale, PA, 1984, pp. 199–209.

[45] F.P. Ford, A Mechanism of Environmentally Controlled Crack-Growth of Structural Steels in High Temperature Water, General Electric Co., Report 81CRD125, Schenectady, NY, 1981.

[46] P.S. Maiya, Prediction of environmental and strain-rate effects on the stress corrosion cracking of austenitic stainless steels, J. Pressure Vessel Technol. 109 (1987) 116–123.

[47] D.P.G. Lidbury, Estimation of crack tip strain rate parameters characterising environment assisted crack growth data, in: R.P. Gangloff (Ed.), Embrittlement by the Localized Crack Environment, The Metallurgical Society – AIME, Warrendale, PA, 1984, pp. 149–172.

[48] S.A. Serebrinsky, G.S. Duffo, J.R. Galvele, Effect of strain rate on stress corrosion crack velocity: difference between intergranular and transgranular cracking, Corros. Sci. 41 (1999) 191–195.

[49] M.O. Speidel, Corrosion in power generating equipment, in: M.O. Speidel, A. Atrens (Eds.), Proceedings of the Corrosion in Power Generating Equipment, Plenum, New York, 1984, pp. 85–130.

[50] R.M. Magdowski, M.O. Speidel, Clean steels for steam turbine rotors-their stress corrosion cracking resistance, Metall. Trans. A 19A (1988) 1583–1596.

[51] J.C. Scully, The interaction of strain-rate and repassivation rate in stress corrosion crack propagation, Corros. Sci. 20 (1980) 997–1016.

[52] J.F. Newman, The stress corrosion of steel in sodium hydroxide solution: a film-rupture model, Corros. Sci. 21 (1981) 487–503.

[53] D.A. Vermilyea, A. Film Rupture Model, A film rupture model for stress corrosion crack propagation, Corrosion 28 (1972) 471.

[54] F.P. Ford, P. Andresen, Corrosion in nuclear systems: environmentally assist cracking in light water reactors, in: P. Marcus (Ed.), Corrosion Mechanisms in Theory and Practice, Marcel Dekker, New York, 2002, pp. 605–642.

[55] A. Lu, T. Shoji, Unified interpretation of crack growth rates of Ni-base alloys in LWR environments, J. Pressure Vessel Technol. 128 (2006) 318–327.

[56] J.R. Scully, P.J. Moran, The influence of strain on hydrogen entry and transport in a high strength steel in sodium chloride solution, J. Electrochem. Soc. 135 (1988) 1337–1348.

[57] R.M. Rieck, A. Atrens, S. Ramamurthy, J.D. Gates, I.O. Smith, Conceptual model of stress corrosion cracking of low-alloy steels in high-temperature water, in: R.P. Gangloff, M.B. Ives (Eds.), Proceedings of the First International Conference on Environment-induced Cracking of Metals, NACE, Houston, 1990.

[58] A. Atrens, Z.F. Wang, ESEM observations of SCC Initiation for 4340 high strength steel in distilled water, J. Mater. Sci. 33 (1998) 405–415.